J. Fluid Mech. (1995), *vol.* 302, *pp.* 91–115

Stability of mixed-convection flow in a tall vertical channel under non-Boussinesq conditions

By SERGEY A. SUSLOV AND SAMUEL PAOLUCCI

Department of Aerospace and Mechanical Engineering, University of Notre Dame, Notre Dame, IN 46556, USA

(Received 2 March 1995 and in revised form 15 June 1995)

We have examined the linear stability of the fully developed mixed-convection flow in a differentially heated tall vertical channel under non-Boussinesq conditions. The three-dimensional analysis of the stability problem was reduced to an equivalent two-dimensional one by the use of Squire's transformation. The resulting eigenvalue problem was solved using an integral Chebyshev pseudo-spectral method. Although Squire's theorem cannot be proved analytically, two-dimensional disturbances are found to be the most unstable in all cases. The influence of the non-Boussinesq effects on the stability was studied. We have investigated the dependence of the critical Grashof and Reynolds numbers on the temperature difference. The results show that four different modes of instability are possible, two of which are new and due entirely to non-Boussinesq effects.

1. Introduction

When forced convection is superimposed on natural convection, the resulting flow is referred to as mixed convection. In the present work, we study mixed-convection flow in a tall vertical channel whose walls are differentially heated. In such a channel, when the buoyant forces are sufficiently large, reverse flow will occur and subsequently greatly influence the stability of the flow field. Mixed convection flow in a tall vertical channel is a problem of current interest and is frequently encountered in applications such as heat exchangers, electronic equipment, chemical vapour deposition, and nuclear reactors. In many such applications, density (or temperature) differences are so large that non-Boussinesq conditions prevail.

The objective of the present work is to examine the linear stability of mixed convection flow in a differentially heated long vertical channel under non-Boussinesq conditions. All of the analyses performed to date which deal with this problem make use of the Boussinesq approximation. Solution of the resulting Boussinesq equations is generally preferred since they are simpler to solve, and their solution has been shown to provide a good approximation in problems where density variations are small (Gray & Giorgini 1976). Unfortunately, in many of the applications cited above, density variations can be extremely large, thus the Boussinesq approximation is not applicable.

There are a number of published studies that are related to the present investigation. To gain a better perspective of results to be presented, we summarize their primary conclusions.

In the limiting case of zero Reynolds number *Re*, the flow becomes that of pure natural convection. The stability of this flow in the Boussinesq limit has been analysed by a number of investigators (Rudakov 1967; Vest & Arpaci 1969; Hart 1971; Korpela, Gözüm & Baxi 1973; Bergholz 1978; Lee & Korpela 1983; Chen & Pearlstein

1989). The major conclusions are that for Prandtl numbers Pr less that 12.45 the instability is shear driven and stationary, and the Prandtl number dependence is slight. The instability is one in which the disturbance energy is gained from the action of the shear forces in the mean flow resulting from natural convection. For $Pr = 0.71$ the critical Grashof and wave numbers are found to be $Gr_c^0 = 8037$ and $\alpha_c^0 = 2.8$. For Prandtl numbers larger that 12.45, the instability is thermally driven and oscillatory. The instability in this case is one in which the disturbance energy is gathered primarily from the potential energy associated with the buoyant forces.

For reasons that will become evident shortly, we digress to note the relationship between two distinct problems. When the Boussinesq equations are used and $Re = 0$ the velocity distribution is represented by a cubic profile and thus the net mass flux on any horizontal plane is zero. The same problem results from the two different cases consisting of the flow inside a tall channel open to an environment and of the flow within a tall but closed cavity. In the former case, the appropriate condition is that the thermodynamic pressure within the channel must be equal to that of the environment which it is open to. In the latter case, the appropriate condition is that the mass flux along any horizontal plane to zero (Suslov & Paolucci 1995). When properties are allowed to vary (non-Boussinesq case), these two conditions result in distinct problems.

Taking into account only viscosity variations for the flow within a tall but closed cavity, Thangam & Chen (1986) and Chen & Pearlstein (1989) find that the instability is always oscillatory for arbitrary values of Prandtl number. No quantitative information regarding wave speeds is given.

An analysis of the stability of mixed-convection flow to two-dimensional disturbances in the Boussinesq limit has been performed by Fukui *et al.* (1982) for $Pr = 0.7$. They obtain critical Grashof numbers, wave speeds, and wavenumbers for a limited range of Reynolds numbers ($0 \leqslant Re \leqslant 100$). Over this range, the critical Grashof number is well approximated by $Gr_c - Gr_c^0 \approx 0.308Re^2$ (where $Gr_c^0 = 8041.4$ is the value they obtain for $Re = 0$), the critical wave speed is approximately given by $c_c \approx 0.855Re$, and the critical wavenumber α_c decreases monotonically from 2.81 at $Re = 0$ to 2.61 at $Re = 100$. In addition to the analysis, they also performed experiments with air as the working fluid. They find the experimental results to be in excellent agreement with their stability results. Yao & Rogers (1989) analyse the stability of the mixed-convection flow within a vertical annulus whose cylindrical walls are maintained at different temperatures, and whose ratio of inside radius to gap width is 100. In this case, the effect of wall curvature is minimal. They present critical values of $(Gr/Re)_c$, c_c, and α_c for $Pr = 0.71$ and for the extended range $0 \leqslant Re \leqslant 1.4 \times 10^4$. Since their emphasis is on large values of the Reynolds number, it is difficult to compare their results with those of Fukui *et al.* (1982) within their common Reynolds number range. For $Re > 0$ they always find the instability to be oscillatory and resulting from shear due to the basic flow. However, they distinguish three modes of instability: the 'thermal mode' for small Reynolds number and large Grashof number (since the basic flow results primarily from buoyancy), the 'shear' mode for small Grashof number (since in this case the basic flow results from imposed pressure gradients), and the 'interaction' mode (for the region where the basic flow depends on both physical mechanisms).

In the present work we use the low-Mach-number approximation to the compressible equations. A detailed discussion of properties of these equations along with their derivation are given by Paolucci (1982). A brief discussion directly relevant to the present problem is given in the next section.

The paper is organized as follows. First we formulate the problem to be studied. This is followed by a description of the basic flow which is an exact solution of the problem. It is shown that regions of counter flow exist for a limited range of Grashof and Reynolds numbers. We next formulate the linear stability problem of this flow, and subsequently solve the resulting perturbation equations using an integral Chebyshev pseudo-spectral method. The primary conclusions of the study for $Pr = 0.71$ are that: (i) the instability is almost always oscillatory; (ii) for temperature differences smaller than a critical value, the instability is always shear driven but the character changes as a function of Reynolds number in a way similar to that found by Yao & Rogers (1989); (iii) for temperature differences greater than a critical value, a new mode of instability (due entirely to non-Boussinesq effects) is found which is purely thermal in character in that the disturbance energy is gained from the potential energy associated with the buoyant forces, and is analogous to but not the same as the type of instability found for $Pr > 12.45$ in the Boussinesq case; (iv) there exists a critical Reynolds number in the non-Boussinesq regime at which the instability switches between different modes associated with shear.

2. Problem formulation

Consider the flow of a gas in a channel consisting of two long vertical parallel plates. The distance between the plates is H. The x^*-coordinate is fixed on the left wall, and the y^*-coordinate is positive in the upwards direction. The left and right walls of the channel are maintained at temperatures T_h^* and T_c^* respectively, where $T_h^* \geqslant T_c^*$, and a pressure gradient $\mathrm{d}\Pi^*/\mathrm{d}y^*$ is imposed in the vertical direction. Asterisk superscripts denote dimensional quantities.

We non-dimensionalize the problem with reference quantities for length, velocity, temperature, and thermodynamic pressure using the channel width H, the viscous diffusion speed $u_r = \nu_r/H$, the average temperature $T_r = (T_h^* + T_c^*)/2$, and the ambient thermodynamic pressure P_r, respectively:

$$\left.\begin{array}{c} x_i^* = Hx_i, \quad t^* = (H/u_r)\,t, \quad u_i^* = u_r u_i, \quad T^* = T_r T, \\ P^* = P_r P, \quad \rho^* = \rho_r \rho, \quad \Pi^* = \rho_r u_r^2 \Pi, \\ c_p^* = c_{p_r} c_p, \quad \mu^* = \mu_r \mu, \quad k^* = k_r k, \end{array}\right\} \tag{1}$$

where we have introduced the reference density ρ_r, viscosity μ_r, thermal conductivity k_r, and specific heat at constant pressure c_{p_r}, all evaluated at the reference temperature and thermodynamic pressure.

The resulting dimensionless governing equations, valid under low-Mach-number conditions, but allowing for arbitrary density variations, are given as follows (Paolucci 1982):

$$\frac{\partial \rho}{\partial t} + \frac{\partial \rho u_i}{\partial x_i} = 0, \tag{2}$$

$$\frac{\partial \rho u_i}{\partial t} + \frac{\partial \rho u_j u_i}{\partial x_j} = -\frac{\partial \Pi}{\partial x_i} + \frac{Gr}{2\epsilon}(\rho - 1)\, n_i + \frac{\partial \tau_{ij}}{\partial x_j}, \tag{3}$$

$$\rho c_p \left(\frac{\partial T}{\partial t} + u_j \frac{\partial T}{\partial x_j}\right) = \frac{1}{Pr}\frac{\partial}{\partial x_j}\left(k \frac{\partial T}{\partial x_j}\right), \tag{4}$$

$$\rho T = 1, \tag{5}$$

where $u_i = (u, v, w)$ are velocity components in the $x_i = (x, y, z)$ directions respectively, $\Pi(x_i, t) = p(x_i, t) - 1 - (Gr/2\epsilon)\, x_i n_i$ is a reduced pressure which accounts for hydrodynamic effects, $n_i = (0, -1, 0)$ is the unit vector in the direction of gravity, and τ_{ij} is the viscous stress tensor given by

$$\tau_{ij} = \mu\left(\frac{\partial u_i}{\partial x_j}+\frac{\partial u_j}{\partial x_i}\right)-\tfrac{2}{3}\delta_{ij}\mu\frac{\partial u_k}{\partial x_k}, \tag{6}$$

where δ_{ij} is the Kronecker delta. Boundary conditions at the vertical walls are given by

$$u_i = 0, \quad T = 1+\epsilon \quad \text{at} \quad x = 0 \quad \text{and} \quad u_i = 0, \quad T = 1-\epsilon \quad \text{at} \quad x = 1. \tag{7}$$

The independent dimensionless parameters appearing in the equations are respectively the Grashof number, the temperature difference, and the Prandtl number:

$$Gr = \frac{\beta_r g \Delta T H^3}{\nu_r^2}, \quad \epsilon = \tfrac{1}{2}\beta_r \Delta T, \quad Pr = \frac{\nu_r}{\alpha_r}. \tag{8}$$

In the above definitions $\Delta T = T_h^* - T_c^*$ and we have introduced the coefficient of thermal expansion $\beta_r = 1/T_r$, the kinematic viscosity $\nu_r = \mu_r/\rho_r$, the thermal diffusivity $\alpha_r = k_r/\rho_r c_{p_r}$, and the magnitude of the gravitational field g. We note that since the channel is open to an atmosphere, we have the choice of maintaining either a constant mass flux or a constant longitudinal pressure gradient within the channel. In this work we choose to maintain a constant longitudinal pressure gradient. Related to this imposed pressure gradient, a Reynolds number is defined as

$$Re = \frac{U_r H}{\nu_r}, \tag{9}$$

where

$$U_r = -\frac{H^2}{12\mu_r}\frac{\mathrm{d}\bar{\Pi}^*}{\mathrm{d}y^*} = \langle \bar{v}^* |_{\epsilon\to 0}\rangle \tag{10}$$

is a characteristic speed of the resulting flow and $\mathrm{d}\bar{\Pi}^*/\mathrm{d}y^*$ corresponds to the imposed pressure gradient. Note that U_r corresponds to the mean velocity of the mixed convection flow in the Boussinesq limit ($\epsilon \to 0$) and the angle brackets denote the average of the quantity over the layer. We emphasize that U_r is related to the constant dynamic pressure gradient and not to the actual mean velocity of the mixed-convection flow for finite values of ϵ. Furthermore, the condition $Re = 0$ means that the dynamic pressure gradient is zero, but it does not say anything about the total mass flux for finite ϵ (however we do know that the mass flux is zero in the Boussinesq limit).

The dimensionless energy equation and equation of state reflect the fact that the thermodynamic pressure is constant inside the channel. In addition we assume that the gas is calorically perfect so that

$$c_p = 1. \tag{11}$$

To account for local variations in transport properties, the dimensionless dynamic viscosity and thermal conductivity are given by the Sutherland-law forms

$$\mu = T^{3/2}\left(\frac{1+S_\mu}{T+S_\mu}\right), \quad k = T^{3/2}\left(\frac{1+S_k}{T+S_k}\right). \tag{12}$$

For air at $T_r = 300$ K and normal pressure, the dimensionless Sutherland constants are (White 1974) $S_\mu = S_\mu^*/T_r = 0.368$ and $S_k = S_k^*/T_r = 0.648$.

From the definition of ϵ we note that $0 \leqslant \epsilon < 1$ corresponds to the temperature difference range of $0 \leqslant \Delta T < \infty$. Obviously the range of validity of the Sutherland law is considerably less. As a point of reference, note that $\epsilon = 0.6$ corresponds to $T_h^* =$

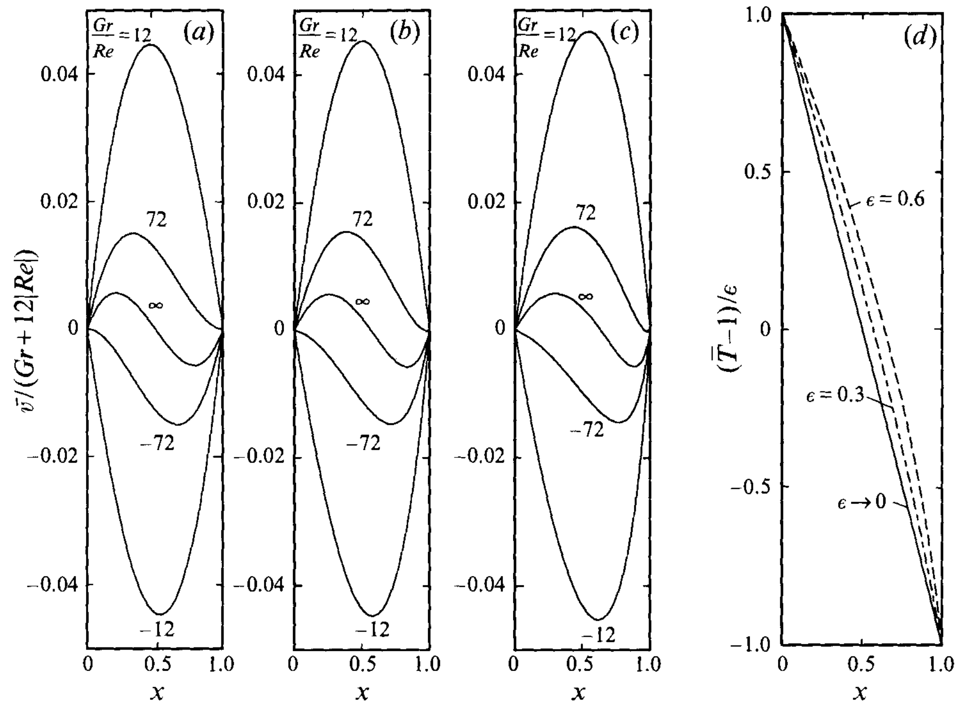

FIGURE 1. Basic flow solution: velocity for several values of Gr/Re and for (*a*) $\epsilon \ll 1$, (*b*) $\epsilon = 0.3$, (*c*) $\epsilon = 0.6$, and (*d*) temperature for the same values of ϵ.

480 K and $T_c^* = 120$ K for $T_r = 300$ K, and represents an accurate upper limit on the validity of the results for air resulting from increasing errors in the Sutherland law conductivity at the cold wall. For the above temperature range, and if f represents any of the properties (ρ, μ, k, c_p, Z) (where Z is the compressibility factor) and $\Delta f = f_h - f_c$, from Hilsenrath *et al.* (1960) we find that $\Delta\rho \approx 190\%$, $\Delta\mu \approx 96\%$, $\Delta k \approx 107\%$, $\Delta c_p \approx 1\%$, and $\Delta Z \approx 1\%$, which fully justify the approximations (12) and assumptions (11) and (5). As an alternative formulation, and using our non-dimensionalization, we could have introduced property contrasts as done in weak non-Boussinesq analyses (see Busse 1967) by taking $f = 1 + (\Delta f/2\epsilon)(T-1)$. However, no benefit is gained since this formulation does not lead to a reduction in the number of dimensionless parameters, while at the same time the applicability of the results for a specific fluid would be over a much more limited temperature difference range since one then cannot account for the nonlinear variations with temperature.

Finally, let us emphasize the following points. While at first glance the governing equations appear to be the same as the conventional compressible equations with variable properties, they are not. The fundamental difference, which arises from a low-Mach-number expansion of the compressible equations, is the decoupling of the pressure into two components: one which contains all hydrodynamic and hydrostatic effects and the other the thermodynamic effects. The latter is normally the ambient thermodynamic pressure if the channel is open (and unity due to the normalization if the ambient thermodynamic pressure is constant), otherwise it is just the average pressure within the channel. Subsequently, it can be shown that acoustic waves are not contained in equations (2)–(5), and $\Pi(x_i, t)$ has elliptic character. We now contrast these equations to the classical Boussinesq equations. In our equations we have present the dimensionless temperature difference ϵ. It can be shown (see Paolucci 1982) that in the mathematical limit $\epsilon \rightarrow 0$ (which corresponds to the physical statement $\epsilon \ll 1$) our equations reduce to the Boussinesq equations in which all properties are constant with the exception of linear density variations in the buoyancy terms. In comparing with the Boussinesq equations, we have four properties which vary with temperature in a consistent manner for a specified fluid (in our case air): the density, the dynamic viscosity, the thermal conductivity, and the specific heat at constant pressure. Over the temperature range investigated, the density, dynamic viscosity, and thermal conductivity of air are all accurately modelled by the ideal gas law and Sutherland law formulations. In addition, over the same temperature range, the specific heat at constant pressure can be approximated by a constant value. It is important that all properties be modelled accurately since it has been shown (see Chenoweth & Paolucci 1985) that the flow can be very sensitive to the individual property variations. Thus only when all properties are consistently modelled can one expect to obtain physically relevant results. In the present work all properties are accounted for properly within the temperature range used.

3. Basic flow

In the region located far enough away from the ends of the channel (the entry length depends strongly on the parameters and is discussed by Aung & Worku (1986) and Chenoweth & Paolucci (1986)) a fully developed flow can exist. For such a flow $\bar{u}_i = (0, \bar{v}(x), 0)$, $\bar{T} = \bar{T}(x)$, and $\bar{\Pi} = \bar{\Pi}(y)$, where $\mathrm{d}\bar{\Pi}/\mathrm{d}y = -12\, Re$, so that the steady-state problem reduces to

$$\frac{\mathrm{d}}{\mathrm{d}x}\left(\bar{\mu}\frac{\mathrm{d}\bar{v}}{\mathrm{d}x}\right) = \frac{Gr}{2\epsilon}(\bar{\rho}-1) - 12Re, \tag{13}$$

$$\frac{\mathrm{d}}{\mathrm{d}x}\left(\bar{k}\frac{\mathrm{d}\bar{T}}{\mathrm{d}x}\right) = 0, \tag{14}$$

$$\bar{\rho}\bar{T} = 1, \tag{15}$$

$$\bar{v} = 0, \quad \bar{T} = 1+\epsilon \quad \text{at} \quad x = 0 \quad \text{and} \quad \bar{v} = 0, \quad \bar{T} = 1-\epsilon \quad \text{at} \quad x = 1, \tag{16}$$

where, using (12), we have $\bar{\mu} = \mu(\bar{T})$ and $\bar{k} = k(\bar{T})$. The solution of these equations is (Chenoweth & Paolucci 1986)

$$x = \frac{f_h - f}{f_h - f_c}, \tag{17}$$

$$\bar{v} = \frac{\beta}{Q^2}\left(\frac{1+S_k}{1+S_\mu}\right)\left\{\frac{Gr}{2\epsilon}\left[\omega_c\left(\frac{\omega}{\omega_c} - \frac{\theta}{\theta_c}\right) + S_k(\omega_c - \phi_c)\left(\frac{\omega-\phi}{\omega_c-\phi_c} - \frac{\theta}{\theta_c}\right)\right] + 12Re\, S_k(\omega_c-\phi_c)\left(\frac{\omega-\phi}{\omega_c-\phi_c} - \frac{\theta}{\theta_c}\right)\right\}, \tag{18}$$

where f, β, Q, θ, ϕ, ω are functions of $\bar{T}$ and S_k and are given in Appendix A. It can be shown that the solution in the Boussinesq limit $\epsilon \ll 1$ reduces to

$$\bar{T} = 1 + \epsilon(1-2x), \tag{19}$$

$$\bar{v} = 6Re(x - x^2) + \tfrac{1}{12}Gr(2x^3 - 3x^2 + x), \tag{20}$$

and coincides with one given by Fukui *et al.* (1982). The basic flow solution is displayed in figure 1 for several values of Gr/Re and ϵ.

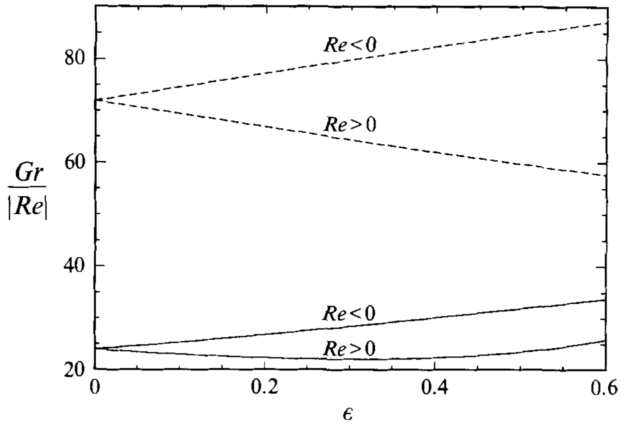

FIGURE 2. Values of Gr/Re which separate regions with and without an inflection point (solid lines) and reverse flow (dashed lines) as functions of ϵ. The inflection point and reverse flow exist for values above the corresponding lines for positive and negative Reynolds numbers.

From figure 1 we see immediately that in general the solution does not have any symmetry with respect to x. This effect is due to the fixed direction of the gravitational field. Only in the Boussinesq limit is the flow centro-symmetric about $x = \frac{1}{2}$ when the sign of the Reynolds number is reversed. Consequently, the cases of positive and negative Reynolds numbers must be considered separately. In addition, even though the total mass flux is zero for $Re = 0$ in the Boussinesq limit, this is not the case when ϵ is finite because of the loss of symmetry resulting from property variations and since we are not imposing any condition on mass flux. Finally, we note that in all cases, as the absolute value of the Reynolds number is increased, the reverse flow disappears and eventually the flow approaches the equivalent variable-property Poiseuille flow. The value of $Gr/|Re|$ at which the reverse flow and the inflection point disappear are given in figure 2 as functions of ϵ. In the Boussinesq limit their values are 72 and 24 respectively. As will be shown later, the type of instability of the basic flow depends on the presence or absence of the inflection point. A more detailed discussion of the basic flow is given by Chenoweth & Paolucci (1986).

Alternatively, the basic flow solution can be obtained numerically using an integral Chebyshev collocation method (Hatziavramidis & Ku 1985; Ku & Hatziavramidis 1984). In this case the problem (13)–(16) is solved over the domain $\hat{x} \in [-1, 1]$ ($\hat{x} = -1+2x$) for convenience. The method can be described as follows. The discrete integral operator W_{ij} is defined by the following relationship:

$$F(\hat{x}) = \int_{-1}^{\hat{x}} f(\xi)\,\mathrm{d}\xi \Leftrightarrow F(\hat{x}_i) = \sum_{j=1}^{N+1} W_{ij} f(\hat{x}_j), \tag{21}$$

with collocation points selected at $\hat{x}_i = \cos[\pi(i-1)/N]$, $1 \leqslant i \leqslant N+1$. Then the solution of the problem can be written in the form

$$\bar{T}_i = (1+\epsilon)e_i - 2\epsilon \sum_{j=1}^{N+1} \frac{W_{ij}}{k(\bar{T}_j)} \Big/ \sum_{j=1}^{N+1} \frac{W_{1j}}{k(\bar{T}_j)}, \tag{22}$$

$$\bar{v}_i = \frac{1}{4} \sum_{j=1}^{N+1} \frac{W_{ij}}{\mu(\bar{T}_j)} \left\{ \sum_{k=1}^{N+1} W_{jk} \left[\frac{Gr}{2\epsilon} \left(\frac{1}{\bar{T}_k} - e_k \right) - 12 Re\, e_k \right] + C e_j \right\}, \tag{23}$$

where $i = 1, \dots, N+1$, $e_i = 1$, and

$$C = -\sum_{j=1}^{N+1} \frac{W_{1j}}{\mu(\bar{T}_j)} \left\{ \sum_{k=1}^{N+1} W_{jk} \left[\frac{Gr}{2\epsilon} \left(\frac{1}{\bar{T}_k} - e_k \right) - 12 Re\, e_k \right] \right\} \Big/ \sum_{j=1}^{N+1} \frac{W_{1j}}{\mu(\bar{T}_j)}. \tag{24}$$

The system of nonlinear equations (22) is solved first using the IMSL routine NEQNF (IMSL Inc. 1989). Subsequently, $\bar{v}_i$ is explicitly evaluated from (23).

It should be noticed that in the Boussinesq case, since the variation of temperature is small, $\mu(\bar{T})$ and $k(\bar{T})$ reduce to constants equal to unity. Taking into consideration the fact that

$$\sum_{j=1}^{N+1} W_{ij} \hat{x}_j^m = [\hat{x}_i^{m+1} + (-1)^m]/(m+1),$$

the *numerical* solution (22) and (23) reduces to the *analytical* solution (19) and (20) evaluated at the collocation points (accounting for the coordinate change):

$$\bar{T}_i = e_i - \epsilon \hat{x}_i, \tag{25}$$

$$\bar{v}_i = -\tfrac{3}{2} Re(\hat{x}_i^2 - e_i) + \tfrac{1}{48} Gr\, \hat{x}_i(\hat{x}_i^2 - e_i). \tag{26}$$

To ensure the accuracy of the numerical method, the non-Boussinesq numerical results were compared with the analytical solution obtained earlier. It has been shown that the discretization error decays exponentially with increasing number of collocation points (Vasilyev & Paolucci 1994). The accuracy of the solution approaches the computer round-off error of 10^{-14} when the number of collocation points reaches 22. We note that in reporting all numerical results in the Boussinesq limit of $\epsilon \ll 1$ we actually use the value of $\epsilon = 10^{-5}$ for the computations.

4. Stability analysis

We now decompose the dependent variables into two parts, the basic flow and a disturbance:

$$\left.\begin{aligned} u_i = \bar{u}_i(x) + u_i'(x,y,z,t), \quad & \rho = \bar{\rho}(x) + \rho'(x,y,z,t), \\ \Pi = \bar{\Pi}(y) + \Pi'(x,y,z,t), \quad & T = \bar{T}(x) + T'(x,y,z,t). \end{aligned}\right\} \tag{27}$$

Substituting (27) into (2)–(5) and (7), subtracting the basic flow solution, making use of the energy equation in the continuity equation, and neglecting second-order disturbance terms, we obtain the following set of equations for the disturbance quantities:

$$\frac{\partial u_j'}{\partial x_j} = \frac{1}{Pr} \frac{\partial}{\partial x_j} \left(\bar{k} \frac{\partial T'}{\partial x_j} + k' \frac{\partial \bar{T}}{\partial x_j} \right), \tag{28}$$

$$\bar{\rho} \left(\frac{\partial u_i'}{\partial t} + \bar{v} \frac{\partial u_i'}{\partial y} + u' \mathrm{D} \bar{u}_i \right) = -\frac{\partial \Pi'}{\partial x_i} + \frac{Gr}{2\epsilon} \rho' n_i + \frac{\partial \tau_{ij}'}{\partial x_j}, \tag{29}$$

$$\bar{\rho} \left(\frac{\partial T'}{\partial t} + \bar{v} \frac{\partial T'}{\partial y} + u' \mathrm{D} \bar{T} \right) = \frac{1}{Pr} \frac{\partial}{\partial x_j} \left(\bar{k} \frac{\partial T'}{\partial x_j} + k' \frac{\partial \bar{T}}{\partial x_j} \right), \tag{30}$$

$$\frac{\rho'}{\bar{\rho}} = -\frac{T'}{\bar{T}}, \tag{31}$$

where $\mathrm{D} \equiv \mathrm{d}/\mathrm{d}x$,

$$\tau_{ij}' = \bar{\mu} \left[\left(\frac{\partial u_i'}{\partial x_j} + \frac{\partial u_j'}{\partial x_i} \right) - \tfrac{2}{3} \delta_{ij} \frac{\partial u_k'}{\partial x_k} \right] + \mu' \left(\frac{\partial \bar{u}_i}{\partial x_j} + \frac{\partial \bar{u}_j}{\partial x_i} \right), \tag{32}$$

and we use the fact that

$$\mu' = \bar{\mu}_T T', \quad k' = \bar{k}_T T', \tag{33}$$

where $\bar{f}_T \equiv \overline{(\mathrm{d}f/\mathrm{d}T)}$. The boundary conditions for the perturbation equations are

$$u_i' = T' = 0 \quad \text{at} \quad x = 0, 1. \tag{34}$$

Next we write the disturbance quantities in the form $f'(x, y, z, t) = \hat{f}(x)\,\mathrm{e}^{\mathrm{i}(\alpha y + \gamma z) + \sigma t}$, where α and γ are the longitudinal and transverse real wavenumbers, and $\sigma = \sigma_R + \mathrm{i}\sigma_I$ is the complex amplification rate. The real and imaginary parts of σ represent the amplification rate of the disturbance and the frequency respectively. The mode is stable, neutrally stable, or unstable depending on whether σ_R is negative, zero, or positive. Now dropping the hats, the system (28)–(31) can be rewritten as a set of linear ordinary differential equations:

$$\mathrm{D}u + \mathrm{i}\alpha v + \mathrm{i}\gamma w = \frac{1}{Pr}[\mathrm{D}(\bar{k}\mathrm{D}T + \bar{k}_T \mathrm{D}\bar{T}T) - \bar{k}(\alpha^2 + \gamma^2)\,T], \tag{35}$$

$$\begin{aligned}\bar{\rho}(\sigma + \mathrm{i}\alpha\bar{v})\,u = -\mathrm{D}\Pi + \{\tfrac{2}{3}\mathrm{D}[\bar{\mu}(2\,\mathrm{D}u - \mathrm{i}\alpha v - \mathrm{i}\gamma w)]& \\ -\bar{\mu}[(\alpha^2 + \gamma^2)\,u - \mathrm{i}(\alpha \mathrm{D}v + \gamma \mathrm{D}w)] + \mathrm{i}\alpha\bar{\mu}_T \mathrm{D}\bar{v}T\},&\end{aligned} \tag{36}$$

$$\begin{aligned}\bar{\rho}(\sigma + \mathrm{i}\alpha\bar{v})\,v + \bar{\rho}\,\mathrm{D}\bar{v}u = -\mathrm{i}\alpha\Pi - \frac{Gr}{2\epsilon}\rho + \{\mathrm{D}[\bar{\mu}(\mathrm{D}v + \mathrm{i}\alpha u) + \bar{\mu}_T \mathrm{D}\bar{v}T]& \\ -\bar{\mu}[(\alpha^2 + \gamma^2)\,v + \tfrac{1}{3}\alpha(2\mathrm{i}\mathrm{D}u + \alpha v + \gamma w)]\},&\end{aligned} \tag{37}$$

$$\bar{\rho}(\sigma + \mathrm{i}\alpha\bar{v})\,w = -\mathrm{i}\gamma\Pi + \{\mathrm{D}[\bar{\mu}(\mathrm{D}w + \mathrm{i}\gamma u)] - \bar{\mu}[(\alpha^2 + \gamma^2)\,w + \tfrac{1}{3}\gamma(2\mathrm{i}\mathrm{D}u + \alpha v + \gamma w)]\}, \tag{38}$$

$$\bar{\rho}(\sigma + \mathrm{i}\alpha\bar{v})\,T + \bar{\rho}\,\mathrm{D}\bar{T}u = \frac{1}{Pr}[\mathrm{D}(\bar{k}\,\mathrm{D}T + \bar{k}_T \mathrm{D}\bar{T}T) - \bar{k}(\alpha^2 + \gamma^2)\,T], \tag{39}$$

$$\rho/\bar{\rho} = -T/\bar{T}. \tag{40}$$

Equations (35)–(39), together with the boundary conditions

$$u_i = T = 0 \quad \text{at} \quad x = 0, 1 \tag{41}$$

constitutes a three-dimensional eigenvalue problem for the complex amplification rate σ. Note that the Reynolds-number dependence enters through the basic flow solution $\bar{v}$.

Now using Squire's transformation

$$\left.\begin{aligned}\tilde{\alpha}\tilde{v} = \alpha v + \gamma w, \quad \tilde{u} = u, \quad \tilde{w} = w, \quad \tilde{T} = T, \quad \tilde{\Pi} = \Pi, \quad \tilde{\alpha}\tilde{y} = \alpha y + \gamma z,\\ \tilde{\alpha}^2 = \alpha^2 + \gamma^2, \quad \tilde{\gamma} = \gamma, \quad \tilde{\sigma} = \sigma, \quad \tilde{\epsilon} = \epsilon, \quad \tilde{Pr} = Pr, \quad \tilde{Gr} = Gr\cos\lambda, \quad \tilde{Re} = Re\cos\lambda,\end{aligned}\right\} \tag{42}$$

where $\lambda = \cos^{-1}(\alpha/\tilde{\alpha})$ is the angle between the transverse direction and the vertical wavenumber, it can be easily shown that equations resulting from (35)–(37) and (39) are independent of $\tilde{w}$ and $\tilde{\gamma}$, while that resulting from (38) depends on all variables. Furthermore, if the equation corresponding to (38) is then multiplied by $\tilde{w}^*$ (the complex conjugate of $\tilde{w}$) and integrated by parts over the width of channel, we obtain

$$\tilde{\sigma} = \tilde{\sigma}_R + \mathrm{i}\tilde{\sigma}_I = -\frac{\langle\bar{\mu}(|\mathrm{D}\tilde{w}|^2 + \tilde{\alpha}^2|\tilde{w}|^2)\rangle}{\langle\bar{\rho}|\tilde{w}|^2\rangle} - \mathrm{i}\tilde{\alpha}\frac{\langle\bar{\rho}\bar{v}|\tilde{w}|^2\rangle}{\langle\bar{\rho}|\tilde{w}|^2\rangle}. \tag{43}$$

Thus the eigenvalue associated with the transverse momentum equation always has a negative real part since $\bar{\rho} > 0$ and $\bar{\mu} > 0$ (Vasilyev & Paolucci 1994). We note then that

ϵ	Re	N	Gr_c	α_c
10^{-5}	13000	42	4.4841024×10^5	2.1063
		43	4.4853575×10^5	2.1060
		45	4.4846939×10^5	2.1060
0.3	-5180	42	5.2696823×10^5	1.1805
		43	5.2696787×10^5	1.1805
		45	5.2696787×10^5	1.1805
0.536	0	20	1.3187455×10^4	0.8884
		30	1.3187473×10^4	0.8884
		39	1.3187473×10^4	0.8884
0.6	-800	20	9.5033539×10^4	0.1000
		30	9.5032304×10^4	0.1000
		39	9.5032304×10^4	0.1000
	88	20	1.8218730×10^4	2.6020
		30	1.8217641×10^4	2.6022
		39	1.8217641×10^4	2.6022

TABLE 1. Convergence of critical parameters for several values of ϵ and Re using different numbers of Chebyshev modes

the reduced eigenvalue problem is identical in form to the problem obtained without the use of Squire's transformation but with $w = \gamma = 0$. Thus we can conclude that the three-dimensional problem is equivalent to a two-dimensional one at smaller Grashof and Reynolds numbers. We emphasize that what we call the equivalent two-dimensional problem (see (44) below) is still three-dimensional through the parameter λ. Thus, it does not follow that Squire's theorem holds (Vasilyev & Paolucci 1994). Consequently, in order to obtain results for the three-dimensional problem we have to solve the equivalent two-dimensional one resulting from (35)–(37), (39), and (41). From the solution of this problem we can then derive the required solution of the three-dimensional problem by varying λ.

As done in the numerical solution of the basic flow, we solve the eigenvalue problem in the domain $\tilde{x} \in [-1, 1]$. Using discrete integral and differential operators (Hatziavramidis & Ku 1985; Ku & Hatziavramidis 1984), the eigenvalue problem can be rewritten in discrete form as

$$\boldsymbol{A}X = \tilde{\sigma}\boldsymbol{B}X, \tag{44}$$

where

$$X = (\tilde{u}''_1, \ldots, \tilde{u}''_{N+1}, \tilde{v}''_1, \ldots, \tilde{v}''_{N+1}, \tilde{T}''_1, \ldots, \tilde{T}''_{N+1}, \tilde{\Pi}_1, \ldots, \tilde{\Pi}_{N+1})^T, \tag{45}$$

primes denote derivatives with respect to x, and $\boldsymbol{A}$ and $\boldsymbol{B}$ are the $[4(N+1)] \otimes [4(N+1)]$ matrices obtained from pseudo-spectral discretization. The eigenvalues $\tilde{\sigma}$ are then obtained using the IMSL routine GVLCG (IMSL Inc. 1989).

For fixed parameters α, $\tilde{Re}$, and $\tilde{\epsilon}$ the values of $\tilde{Gr}$ and $\tilde{\sigma}_I$ at which $\tilde{\sigma}_R = 0$ are found. Repeating such a procedure for different values of $\tilde{\alpha}$, we obtain the marginal stability curve, say $\tilde{Gr}_0(\tilde{\alpha}, \tilde{Re}, \tilde{\epsilon})$ and the corresponding frequency $\tilde{\sigma}_{I_0}(\tilde{\alpha}, \tilde{Re}, \tilde{\epsilon})$. Critical values $\tilde{Gr}_c(\tilde{\alpha}_c, \tilde{Re}, \tilde{\epsilon}) = \min_{\tilde{\alpha}} \tilde{Gr}_0(\tilde{\alpha}, \tilde{Re}, \tilde{\epsilon})$ and $\tilde{\sigma}_{I_c}(\tilde{\alpha}_c, \tilde{Re}, \tilde{\epsilon})$, and thus also the critical wave speed $\tilde{c}_c = -\tilde{\sigma}_{I_c}/\tilde{\alpha}_c$ are then obtained for specified values of $\tilde{Re}$ and $\tilde{\epsilon}$. The procedure is repeated by varying the Reynolds number in the range $|\tilde{Re}| \leqslant 4 \times 10^4$ for the temperature parameter range between the Boussinesq limit($\tilde{\epsilon} \ll 1$) and $\tilde{\epsilon} = 0.6$ Results of these calculations using the above procedure and the previously noted parameter values appropriate for air are presented next. In addition, all results have been obtained using anywhere from 39 to 51 Chebyshev modes (the higher number is necessary for larger absolute values of Reynolds numbers), and all values are believed to be correct to the significant figures reported. To demonstrate convergence of the results, in table 1 we present critical parameter values obtained for several values of ϵ and Re using different numbers of modes. These parameter values will later be seen to be near where interesting changes in type of instability will occur.

5. Results

As stated in the previous section, the transformation (42) can be used to obtain the three-dimensional results once the equivalent two-dimensional stability problem is solved. In the two limits of either plane pure forced-convection flow or pure natural-convection flow Squire's theorem can be proved even in the non-Boussinesq regime, thus predicting that two-dimensional disturbances are the most unstable. However, for the complete parameter space examined, where Squire's theorem cannot be proved, we have obtained the three-dimensional results by varying λ, and we have found that in all cases the three-dimensional flow was most unstable for $\lambda = 0$ which corresponds to two-dimensional transverse rolls. Thus, we have demonstrated that in all cases the flow is most unstable to two-dimensional disturbances. Subsequently, in presenting all results, we drop the tilde accent, reflecting the above finding.

In figure 3 we show results corresponding to $Re = 0$ as functions of ϵ. From the marginal stability curves shown in figure 3(*a*) we see that as the temperature difference parameter is increased, at first the only effect appears to be a shift of the marginal curve to higher values of Grashof numbers. This leads to larger values of Gr_c as shown in figure 3(*b*). For the temperature difference parameter range of $0 < \epsilon \leqslant \epsilon_*$, where $\epsilon_* = 0.536$, the critical Grashof number can be well approximated by $Gr_c/Gr_c^0 = 1+1.382\epsilon^2+2.780\epsilon^4$, where $Gr_c^0 = 8037.5944$. The increase of Gr_c is accompanied by a slight decrease in the critical wavenumber α_c from the value of $\alpha_c^0 = 2.810$ in the Boussinesq limit as shown in figure 3(*c*). One important point to note, which can be seen from figure 3(*d*), is that the critical wave speed is zero *only* in the Boussinesq limit. For the range $0 < \epsilon \leqslant \epsilon_*$ the critical wave speed is well approximated by $c_c/Gr_c = -4.4 \times 10^{-3}\epsilon$ (it can be shown that the specific constant is a function of Prandtl number and the dimensionless Sutherland constants). This result can be explained by inviscid stability theory as follows. Based on the numerical results for $Pr = 0.71$, it appears (see below) that this instability mechanism is shear driven and possibly linked to the presence of an inflection point in the basic velocity profile (see Lin 1955). Indeed, it can be shown that in the limit $Pr \rightarrow 0$ equation (44) has a singularity at the location where the wave speed equals the basic flow velocity. This singularity is removable however (as it should be) if the basic flow velocity profile has an inflection point at the same location. This is exactly the same situation as in the Boussinesq limit. Note however that in the Boussinesq limit this singularity occurs at $x = \frac{1}{2}$ where the basic velocity is zero and thus the wave speed is also zero; this location also corresponds to the location of the inflection point of the basic velocity profile. However, when properties in the basic flow are allowed to vary, the location of the inflection point, and subsequently the location of the critical layer, is given by

$$x_c \approx \left(\tfrac{1}{2}+12\frac{Re}{Gr}\right)+\left[2.874\times10^{-1}-3.059\times10^{2}\left(\frac{Re}{Gr}\right)^2\right]\epsilon + \left[1.279+8.160\times10^{3}\left(\frac{Re}{Gr}\right)^2\right]\frac{Re}{Gr}\epsilon^2+O(\epsilon^3), \qquad (46)$$

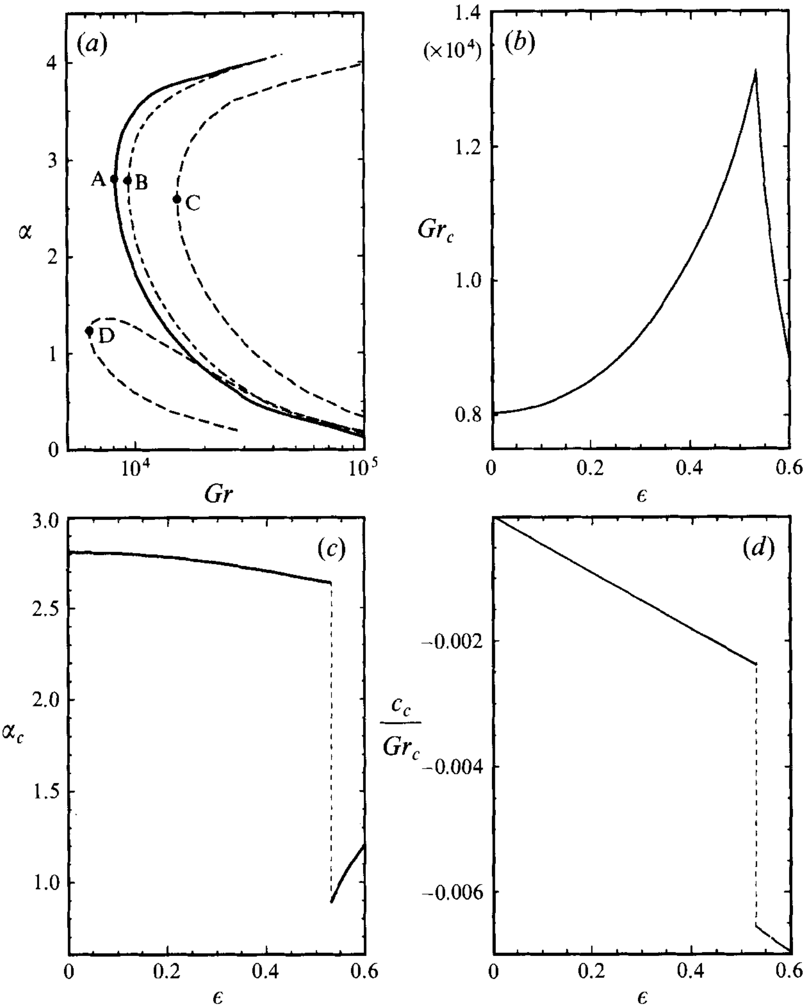

FIGURE 3. (*a*) Marginal stability curves for $\epsilon \ll 1$ (——), $\epsilon = 0.3$ (– – –), and $\epsilon = 0.6$ (----), and (*b–d*) critical parameters as functions of ϵ for $Re = 0$.

and the basic flow velocity at this location, and thus the wave speed, is given in this limit by

$$\frac{c_c}{Gr} \approx -3.136\times 10^{-3}\epsilon + \frac{Re}{Gr}\left\{1 - 576\left(\frac{Re}{Gr}\right)^2 - \left[1.018\times 10^{+1} - 2.038\times 10^{4}\left(\frac{Re}{Gr}\right)^2\right]\frac{Re}{Gr}\epsilon \right.$$
$$\left. - \left[1.070\times 10^{-1} + 7.618\times 10^{+1}\left(\frac{Re}{Gr}\right)^2 + 6.676\times 10^{5}\left(\frac{Re}{Gr}\right)^4\right]\epsilon^2\right\} + O(\epsilon^3), \quad (47)$$

where the constants in (46) and (47) are functions of Pr, S_μ and S_k, but their dependences are too complicated to be given here. Note that for $Re = 0$ and to leading order in ϵ, the wave speed obtained through stability analysis given earlier is in reasonable agreement with the value given in (47) resulting from inviscid arguments. For $Pr > 0$, owing to the contribution of viscous terms, the location of the critical layer is not the same as the location of the inflection point, but the two locations are found to be very close to each other. We stress the fact that the classical result that the

Point	Σ_{Π}	Σ_{uv}	$(Gr/2\epsilon)\Sigma_B$
A	0.0000	0.9418	0.0582
B	0.0006	0.9531	0.0463
C	−0.0028	0.9902	0.0126
D	−0.1465	0.4593	0.6872
E	−0.0779	0.4714	0.6065
F	0.0316	0.9475	0.0209
G	−0.0420	1.0161	0.0259
H	−0.2914	0.4607	0.8307
I	0.0122	0.9942	−0.0064
J	−0.0259	0.9891	0.0368

TABLE 2. Disturbance kinetic energy terms for different values of critical parameters labelled A–D in figure 3, E and F in figure 5, G and H in figure 8, and I and J in figure 7

instability is stationary for $Pr < 12.45$ is only because all property variations are neglected. When property variations are included, the basic flow does not retain the odd symmetry about $x = \frac{1}{2}$. Note that any mechanism which breaks the odd symmetry could possibly change the instability mechanism from stationary to oscillatory. In a study of instability in a differentially heated tall vertical annulus by Choi & Korpela (1980) and Lee, Korpela & Horne (1982) the odd symmetry was broken by the annulus curvature parameter. In their case a similar observation was made in that the instability was oscillatory for any finite value of the curvature parameter. However, the details are very different in their case: the resulting wave speed is in the opposite direction as ours; the location of the critical layer does not coincide with the location of the inflection point of the basic flow; and lastly the parameter breaking the symmetry is a geometric one while in our case it is a physical one. At $\epsilon \approx 0.475$ we first observe the appearance of a secondary branch at low wavenumbers in the marginal stability curve, and as ϵ is increased past ϵ_* the critical parameters switch to this lower branch. This switching at ϵ_* is responsible for the change in behaviour of Gr_c and the abrupt changes in α_c and c_c seen in figure 3(*b–d*). We note that our values of the critical parameters in the Boussinesq limit are in excellent agreement with the values of $Gr_c^0 = 8037$ and $\alpha_c^0 = 2.81$ obtained by Chait & Korpela (1988). Furthermore, the result that the instability becomes oscillatory when property variations are accounted for is consistent with the results of Thangam & Chen (1986) and Chen & Pearlstein (1989).

To understand the physical mechanisms responsible for the two different modes of instability, we will look at the two-dimensional ($w = \gamma = 0$) disturbance kinetic and thermal potential energy balances, $E_{KE} = \frac{1}{2}\langle\bar{\rho}(|u|^2+|v|^2)\rangle$ and $E_{PE} = \frac{1}{2}\langle\bar{\rho}|T|^2\rangle$, respectively. Multiplying (36) by u^* and (37) by v^*, adding them together, and multiplying (39) by T^*, integrating the two resulting equations over the interval $0 \leqslant x \leqslant 1$, and taking the real parts we get

$$\sigma_R E_{KE} = \Sigma_{\Pi} + \Sigma_{uv} + \frac{Gr}{2\epsilon}\Sigma_B + \Sigma_{\mu}, \tag{48}$$

$$\sigma_R E_{PE} = \Sigma_{Tu} + \frac{1}{Pr}\Sigma_k, \tag{49}$$

where all the terms on the right-hand sides are defined in Appendix B. We see that the time rate of change of the disturbance kinetic energy $\sigma_R E_{KE}$ is the sum of contributions due to compressibility effects Σ_{Π}, productions due to shear Σ_{uv} and buoyancy

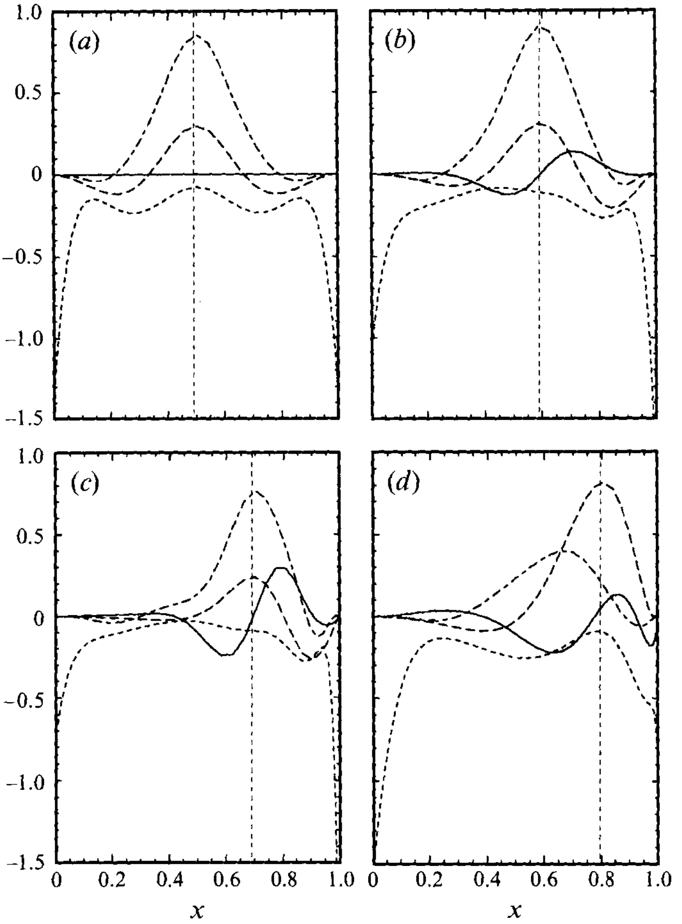

FIGURE 4. Distributions of integrands appearing in the disturbance kinetic energy balance equation: σ_Π (——), σ_{uv} (— — —), $(Gr/2\epsilon)\sigma_B$ (– – –), and σ_μ (----). Plots (*a–d*) correspond respectively to critical points A–D shown in figure 3(*a*). Vertical dotted lines denote the location of the critical layer.

$(Gr/2\epsilon)\Sigma_B$, and viscous dissipation Σ_μ, while the time rate of change of disturbance thermal potential energy $\sigma_R E_{PE}$ depends on the balance between the term Σ_{Tu} which corresponds to the interaction between basic flow temperature gradient and perturbed velocity, and thermal diffusion Σ_k/Pr. The relative values for the different terms entering the disturbance kinetic energy equation for the critical points labelled A–D in figure 3(*a*) are presented in table 2 (note that at these points $\sigma_R = 0$). Since the amplitude of the disturbance is arbitrary in a linear analysis, the normalization is done in such a way that $\Sigma_\mu = -1$. In figure 4 we also present the distributions of the integrands of the disturbance kinetic energy equation correspondingly denoted by σ_Π, σ_{uv}, $(Gr/2\epsilon)\sigma_B$, and σ_μ. Note that the scales on the individual plots are arbitrary, thus one can only compare the relative energy contributions within each such plot. We can see that for Boussinesq and slightly non-Boussinesq regimes (corresponding to points A and B in figure 3*a*) the instability is a shear-driven one, where the disturbance derives its energy from the shear of the basic flow which is largest near the centre of the channel. In addition we see that the maximum shear production always occurs near the location of the critical layer, i.e. the location where the disturbance wave speed is equal to the local basic flow speed. In cases where the instability is shear driven, as noted earlier, the critical layer is located very close to the inflection point of the basic flow given by equation (46), which in turn moves towards the cold wall as ϵ increases. We should also note the fact that while compressibility effects do not contribute much to the disturbance kinetic energy balance in the integral sense in the weak non-Boussinesq regime (see table 2, point B), it does not mean that the disturbances are incompressible (see figure 4*b*). When $\epsilon > \epsilon_*$ the disturbance derives the majority of its kinetic energy from the thermal interaction with the basic flow density field through buoyancy, hence resulting in a buoyant instability. The appearance of this new mode of instability is explained as follows. First we note that the local buoyancy contribution to the kinetic energy of the disturbance is given by

$$\frac{Gr}{2\epsilon}\sigma_B = Gr\frac{1}{2}\frac{1}{(1+2\epsilon\bar{\theta})^2}(\theta v^*)_R, \tag{50}$$

where we have rescaled the temperature to remove the ϵ dependence from the boundary conditions by using the relation $\theta = (T^* - T_r)/(T_h^* - T_c^*) = (T-1)/2\epsilon$ (so that $\bar{\theta} = \pm\frac{1}{2}$ at $x = 0, 1$). Furthermore, we note that

$$\bar{\theta} = \left(\frac{1}{2} - x\right) + \frac{1}{2}\left(\frac{1+3S_k}{1+S_k}\right)x(1-x)\,\epsilon + O(\epsilon^2). \tag{51}$$

Now in the Boussinesq limit ($\epsilon \rightarrow 0$) the buoyancy contribution becomes $Gr\frac{1}{2}(\theta v^*)_R$. Since the shear contribution to the disturbance kinetic energy depends linearly on the Grashof number (through the basic flow dependence with $Re = 0$), then for fixed Prandtl number the ratio of the buoyancy contribution to that of the shear is always of the same order of magnitude, which is seen to be numerically small (see table 2 point A for $Pr = 0.71$). On the other hand, when ϵ is finite the buoyancy contribution to the kinetic energy of the disturbance to leading orders in ϵ becomes

$$Gr\frac{1}{2}\left\{\frac{1}{1-2(2x-1)\epsilon+[(2x-1)^2+2[(1+3S_k)/(1+S_k)]\,x(1-x)]\,\epsilon^2}+O(\epsilon^3)\right\}(\theta v^*)_R, \tag{52}$$

which is largest in the vicinity of the cold wall since the term in curly brackets is largest at $x = 1$; however both θ and v^* are zero there. The actual x-location where this term is largest depends on ϵ, S_μ, S_k, and the specific disturbance correlation, which in turn also depends on the Prandtl number. We finally note now that for fixed Prandtl number the ratio of the buoyancy contribution to that of the shear can be increased by increasing ϵ. Thus the buoyancy contribution can be enhanced by either increasing the temperature difference for a specific fluid, or by varying the Prandtl number using different fluids for a fixed temperature difference. Ultimately, for fixed Prandtl number, at ϵ_* the buoyancy contribution becomes larger than that of shear and the mode of instability subsequently switches to a buoyant one. From the above discussion, the switch in mode of instability can be directly traced to the nonlinear density variation. As can be seen from (52), this nonlinearity in turn is due primarily to the nonlinear variation with temperature through the equation of state, and only secondarily through the variable conductivity. When the mode of instability becomes buoyant, we also note that global compressibility effects are significant, albeit stabilizing. In addition, as can be seen from figure 4(*d*) the location of the new critical layer corresponds to the location of maximum disturbance production due to buoyancy, which is closer to the cold wall than the location of the inflection point of the basic flow. Thus we conclude that the upper and lower marginal stability curves obtained for $\epsilon = 0.6$, and shown in figure 3(*a*), obviously correspond to branches in which shear and

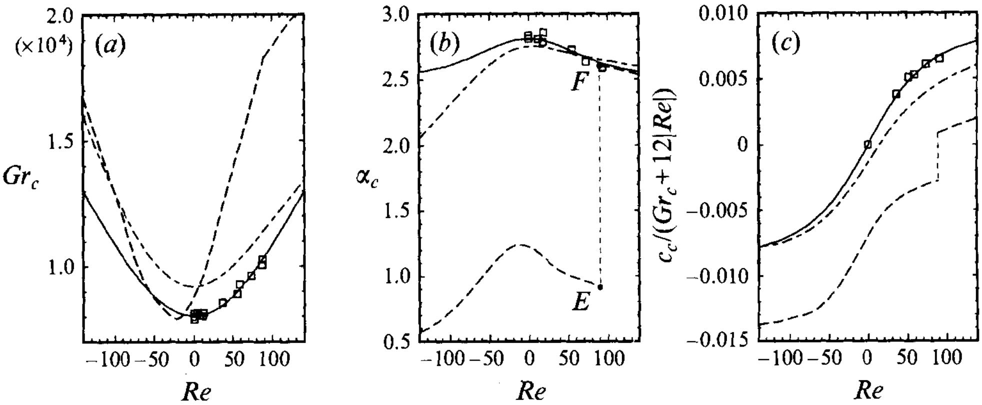

FIGURE 5. Critical parameters for $\epsilon \ll 1$ (——), $\epsilon = 0.3$ (– – – –), and $\epsilon = 0.6$ (– – –) over a small range of Reynolds numbers. Symbols denote experimental data of Fukui *et al.* (1982).

buoyancy production dominate, respectively. We emphasize that the change in mode of instability from one of hydrodynamic origin to one of thermal origin and the corresponding behaviour of the critical parameters are only superficially similar to those observed in the Boussinesq case (Korpela *et al.* 1973) when the Prandtl number is increased past a value of 12.45. The two instabilities are not the same since in our problem the *local* Prandtl number is always less than unity and thus the source of instability is of a different nature.

In figure 5 we show the corresponding critical parameters as functions of Reynolds number for $|Re| \leqslant 140$. In the Boussinesq limit the critical Grashof number, wavenumber, and wave speed are well approximated by $Gr_c - Gr_c^0 = 0.306\ Re^2$, $\alpha_c - \alpha_c^0 = -3.6 \times 10^{-5}\ Re^2$, and $c_c/Re = 0.885 - 450(Re/Gr_c)^2$ over the range of $|Re| < 50$. As can be seen from the figure, our results are in very good agreement with the experimental data of Fukui *et al.* (1982), and with the results of their analysis in which they obtain a value of 0.308 for the critical Grashof number coefficient, and 0.855 for the coefficient of the critical wave speed to leading order in Reynolds number. Furthermore, the constants obtained for the critical wave speed are also in reasonable agreement with the values of 1 and 576 given in (47) which resulted from inviscid arguments. As ϵ is increased first we note that the critical Grashof number is no longer symmetric with respect to the Reynolds number. As ϵ is increased past ϵ_* we further note a qualitative change in the critical Grashof number curve (see the curve corresponding to $\epsilon = 0.6$) and resulting in a substantial drop in the smallest value of Gr_c and corresponding drops of critical wavenumbers and wave speeds. Again we point out that this change is due to a change in the dominant mode of instability from shear driven to buoyantly driven. We note that in the region of Gr–Re parameter space below the critical curves shown in figure 5(*a*), but above the corresponding lines given in figure 2, we have stable reverse flow.

For Boussinesq or slightly non-Boussinesq values of ϵ, as the absolute value of the Reynolds number is increased, the instability continues to be driven by the shear of the basic flow, although the basic flow itself changes from a cubic-like distribution to a parabolic-like distribution. From figures 3 and 4 we noted that at $Re = 0$ there exists a critical ϵ_* such that for $\epsilon < \epsilon_*$ the dominant mode of instability is due to shear, while for $\epsilon > \epsilon_*$ the dominant mode of instability is due to buoyancy. We therefore expect that as the Reynolds number changes, so will the value of ϵ_*. From figure 5 we see that at $Re_*^+ \approx 87.8$, $\epsilon_* = 0.6$. At this Reynolds number, when $\epsilon > \epsilon_*$ the instability is

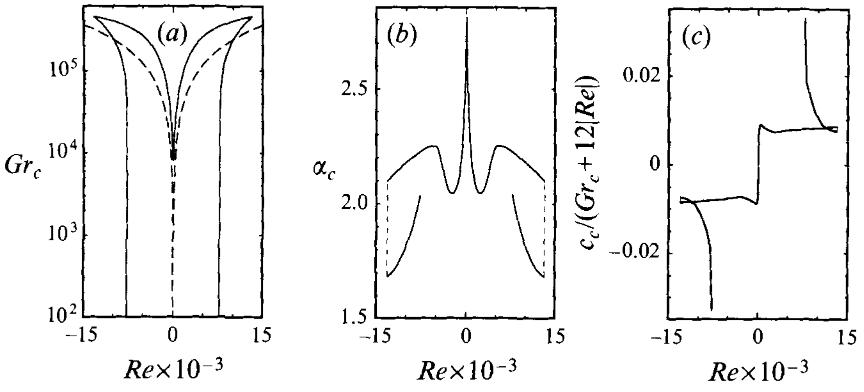

FIGURE 6. Critical parameters for $\epsilon \ll 1$ over a much larger range of Reynolds numbers. The region above the dashed line in (*a*) is where an inflection point is present in the basic flow.

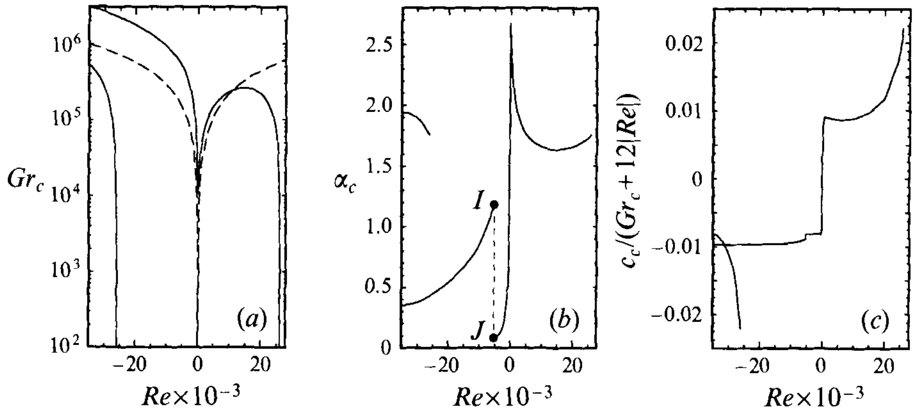

FIGURE 7. Critical parameters for $\epsilon = 0.3$ over a much larger range of Reynolds numbers. The region above the dashed line in (*a*) is where an inflection point is present in the basic flow.

buoyantly driven, while for $\epsilon < \epsilon_*$ it is shear driven. This behaviour is seen by looking at the relative values of the different terms entering the disturbance kinetic energy balance given in table 2 for parameter values in the buoyantly-driven (point E) and shear-driven (point F) regimes. This change is accompanied by corresponding jumps in the critical wavenumbers and wave speeds.

In figures 6–8 we show the critical Grashof number, wavenumber, and wave speed over a much larger range of Reynolds numbers. For details near $Re = 0$ the reader should refer to figure 5. Above the dashed lines in the Gr_c plots are the regions where an inflection point is present in the basic flow. The dotted lines in the figures denote jumps in modes of instability. Furthermore, in figure 9 we show the critical parameters as functions of ϵ corresponding to pure forced convection, i.e. $Gr = 0$. The long–short-dashed lines in the figure denote approximate values of the parameters, since in this regime they were difficult to calculate accurately using the present algorithm.

In the Boussinesq limit we note from figure 6 two branches of the critical parameters on each side of the $Re = 0$ line. These branches intersect at $(Gr_c, |Re|) = (4.5070 \times 10^5, 1.3173 \times 10^4)$. Note that with the exception of a small region below the upper branch, when the basic flow contains an inflection point, the flow is inherently unstable. The marginal stability diagram corresponding to $Re = 1.3173 \times 10^4$ and shown in figure 10 shows the behaviour near the intersection, and is very similar to that obtained recently

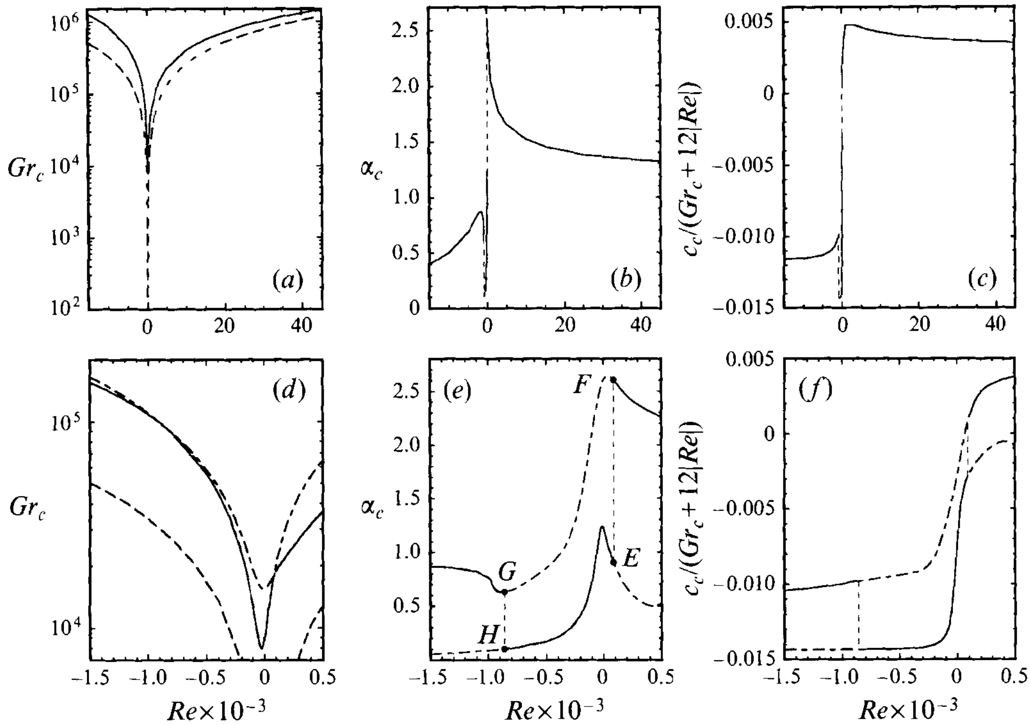

FIGURE 8. Critical parameters for $\epsilon = 0.6$ over a much larger range of Reynolds numbers (*a–c*), and close up in the vicinity of Re_*^- and Re_*^+ (d–f). The regions above the dashed lines in (*a*) and (*d*) are where an inflection point is present in the basic flow. The long–short-dashed lines in (*d*) identify the instability boundaries for the more stable of the two modes.

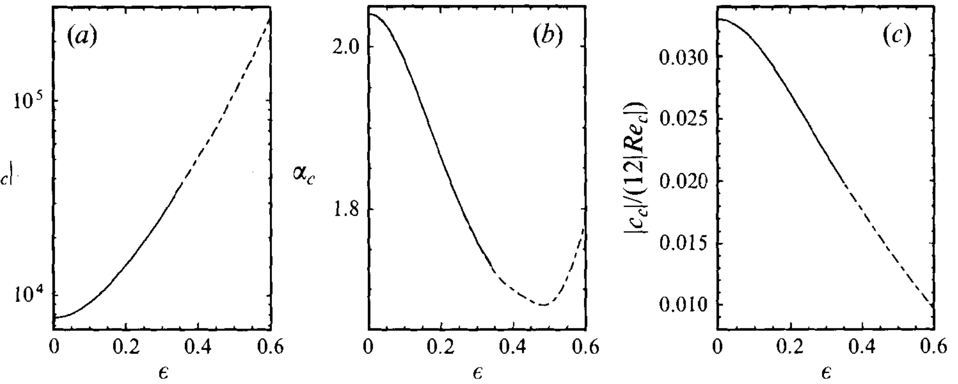

FIGURE 9. Critical (*a*) Reynolds number, (*b*) wavenumber, and (*c*) wave speed as functions of ϵ for $Gr = 0$. The long–short-dashed lines denote approximate values.

by Rogers, Ghosh Moulic & Yao (1993) in their analysis of mixed convection within a concentric annular tube and shown in their figure 4. The branch emanating from $Re = 0$ corresponds to a shear instability of the basic flow arising primarily from the temperature difference across the channel with increasing contribution from pressure gradient effects as the intersection is approached. The second branch also corresponds to a shear instability of the basic flow, but now the contribution to the basic flow arises primarily from the imposed pressure gradient. At parameter values where the two

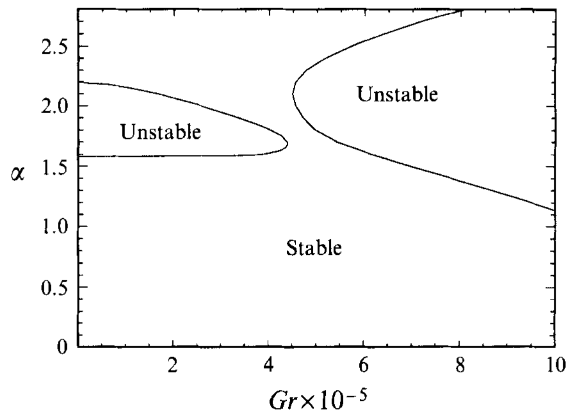

FIGURE 10. Marginal stability diagram for $\epsilon \ll 1$ and $Re = 1.3173 \times 10^4$.

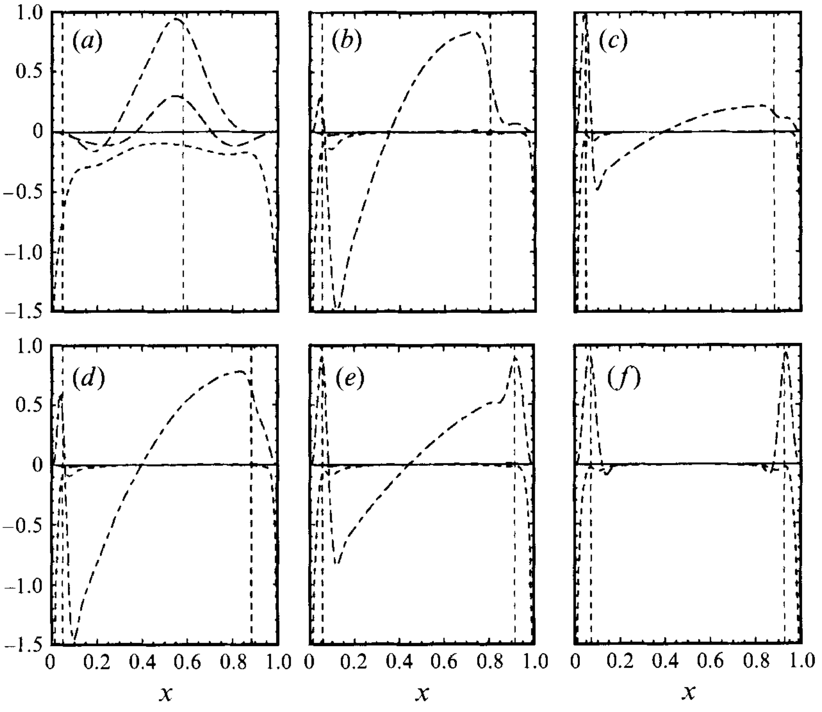

FIGURE 11. Distributions of integrands appearing in the disturbance kinetic energy balance equation: σ_{Π} (——), σ_{uv} (— — —), $(Gr/2\epsilon)\,\sigma_B$ (———), and σ_{μ} (----). The plots correspond to critical values along the upper branch (*a*) $Re = 50$, (*b*) $Re = 4 \times 10^3$, (*c*) $Re = 1.3 \times 10^4$, and along the lower branch (*d*) $Re = 1.3 \times 10^4$, (*e*) $Gr = 1.4 \times 10^5$, (*f*) $Gr = 0$ of figure 6(*a*). Vertical dotted lines denote locations of critical layers.

shear modes switch, we note large jumps in the critical wavenumbers from 2.101 to 1.684 and smaller jumps in critical wave speeds from $c_c = 0.396\ Re$ to $c_c = 0.339\ Re$ as we move from the upper to lower branches. More detail regarding the change in instability is obtained by looking at the change in the distributions of the integrands appearing in the disturbance kinetic energy balance equation as we move along the critical curve shown in figure 6. Their variations are shown in figure 11. From the figure we see the complicated interplay between the instability arising from the critical layer associated with the inflection point, and that associated with the critical layers in the viscous regions. As $Gr \to 0$ the basic flow approaches the plane Poiseuille distribution. In this case we obtain the critical Reynolds number $|Re_c| = 7696.2994$, critical wavenumber $\alpha_c = 2.0410796$, and critical wave speed $|c_c| = 0.3960\ Re_c$. If we rescale the critical Reynolds number and wave speed by the maximum velocity of the basic flow, and the wavenumber by $H/2$ and denote the results by primes, we obtain $|Re_c'| = 5772.2246$, $\alpha_c' = 1.020544$, and $|c_c'| = 0.2640002$. These values are in excellent agreement with those reported by Orszag (1971) and more recently by Davey (unpublished, but see Drazin & Reid 1987, p. 205) who obtained: $Re_c' = 5772.2218$, $\alpha_c' = 1.020547$, and $c_c' = 0.2640003$. Furthermore, our Gr_c–Re parameter space is in excellent agreement with the one computed by Yao & Rogers (1989) (they display theirs in the Gr_c/Re–Re parameter space). We note that for a range of Reynolds numbers somewhat larger than $|Re_c|$ there exist regions where an increase in Grashof number has a stabilizing influence on the predominantly pressure-gradient driven flow. In turn, as the Grashof number is increased further, the flow (which is now primarily due to the temperature difference across the channel) becomes unstable again.

For $\epsilon = 0.3$ we note from figure 7 a large jump in wavenumber and a small one in wave speed at $Re_{**} \approx -5180$ (points I and J). The basic flow profile for Reynolds numbers in this range has an inflection point. As the Reynolds number is decreased from zero we note (although we do not present this here) that secondary rolls start forming near the cold wall and with further decrease of the Reynolds number they ultimately achieve the same strength as the primary rolls. The strong interaction between these rolls eventually leads to an oscillatory disturbance velocity field which is essentially longitudinal ($|u| = O(10^{-2}|v|)$) for Re just greater than Re_{**}. At slightly lower values of Reynolds numbers, this longitudinal disturbance velocity field is drastically altered to one composed of rolls now having a wavelength of more than one order of magnitude smaller. This large change occurring near Re_{**} can be seen clearly by looking at the disturbance fields shown in figure 12. Note that the fields are shown for one wavelength, and their lengths are scaled by their corresponding critical values. (Although not shown here, the corresponding disturbance pressure fields also confirm these drastic changes.) As can be noted from table 2, the switch of instability occurring at Re_{**} is between two shear-driven modes and the role of buoyancy is slightly stabilizing for $Re \lesssim Re_{**}$ (point I) and slightly destabilizing for $Re \gtrsim Re_{**}$ (point J). From figure 1 we see that as $Gr \to 0$ the basic flow approaches a plane Poiseuille-like distribution. For this flow we obtain the following values of critical parameters (see also figure 9): $|Re_c| = 25962$, $\alpha_c = 1.759$, and $|c_c| = 0.266\ Re_c$. For this value of ϵ we note from figure 7(a) that the flow is always unstable for $Re > |Re_c|$. However, similar to the Boussinesq case, there is a range of negative Reynolds numbers below $-|Re_c|$ where for large enough Grashof numbers the flow becomes stable. Upon further increase of Grashof number the flow would eventually become unstable again as in the Boussinesq case. Although outside the range of results shown in the figure, the indication is that for negative Reynolds numbers the switch in modes of instability will be abrupt.

The points where the two stability branches intersect in figure 6(a) correspond to a switch from mixed to shear types of instability, according to Yao & Rogers' (1989) terminology. This switch is found to be very abrupt for $\epsilon < 0.050$ and is smoothed out for positive-Reynolds-number flows for $\epsilon > 0.075$ as shown in figure 7. The investigation of this phenomenon shows that the upper branches of the stability curves shown in figures 6(a) and 7(a) correspond to the inviscid instability associated with the inflection point of the basic flow, while the lower near-vertical branches correspond to

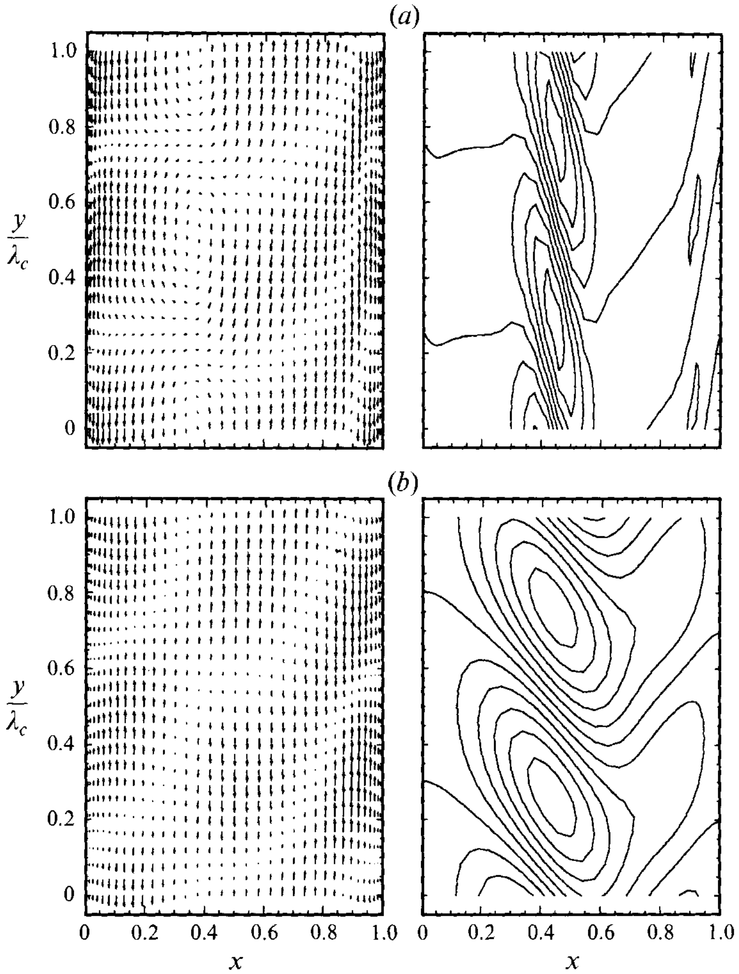

FIGURE 12. Disturbance velocity field and isotherms for $\epsilon = 0.3$, Gr_c, and Re_{**}, corresponding to points (*a*) I and (*b*) J displayed in figure 7. The vertical coordinates are normalized by their corresponding critical wavelengths $\lambda_c = 2\pi/\alpha_c$.

the viscous instability associated with Poiseuille-type flows. The switch occurs when the inflection point reaches the region near a wall where viscous effects become dominant. As seen in the figures, for fixed ϵ as we move along the critical stability curve this switch is sharp or smooth depending on whether an inflection point exists or not for Reynolds numbers whose absolute value is greater than the critical one for pure Poiseuille-like flow. As shown in figure 9, the critical Reynolds number associated with the viscous instability increases rapidly with ϵ. In addition, as can be seen from figures 6(*a*) and 7(*a*), or directly from (46), for fixed ϵ and $|Re/Gr|$ the inflection point moves faster towards the cold wall for $Re/Gr > 0$ than towards the warm wall for $Re/Gr < 0$. For $\epsilon = 0.3$ the inflection point disappears at $Re \approx 10000$, which is much smaller than the critical Reynolds number associated with the viscous instability; consequently, in this case the transition to viscous instability is very smooth. On the other hand for negative Reynolds numbers the inflection point survives past the critical Reynolds number associated with the viscous instability given in figure 9 and thus the switch is sharp (although this is not fully shown in figure 7*a*).

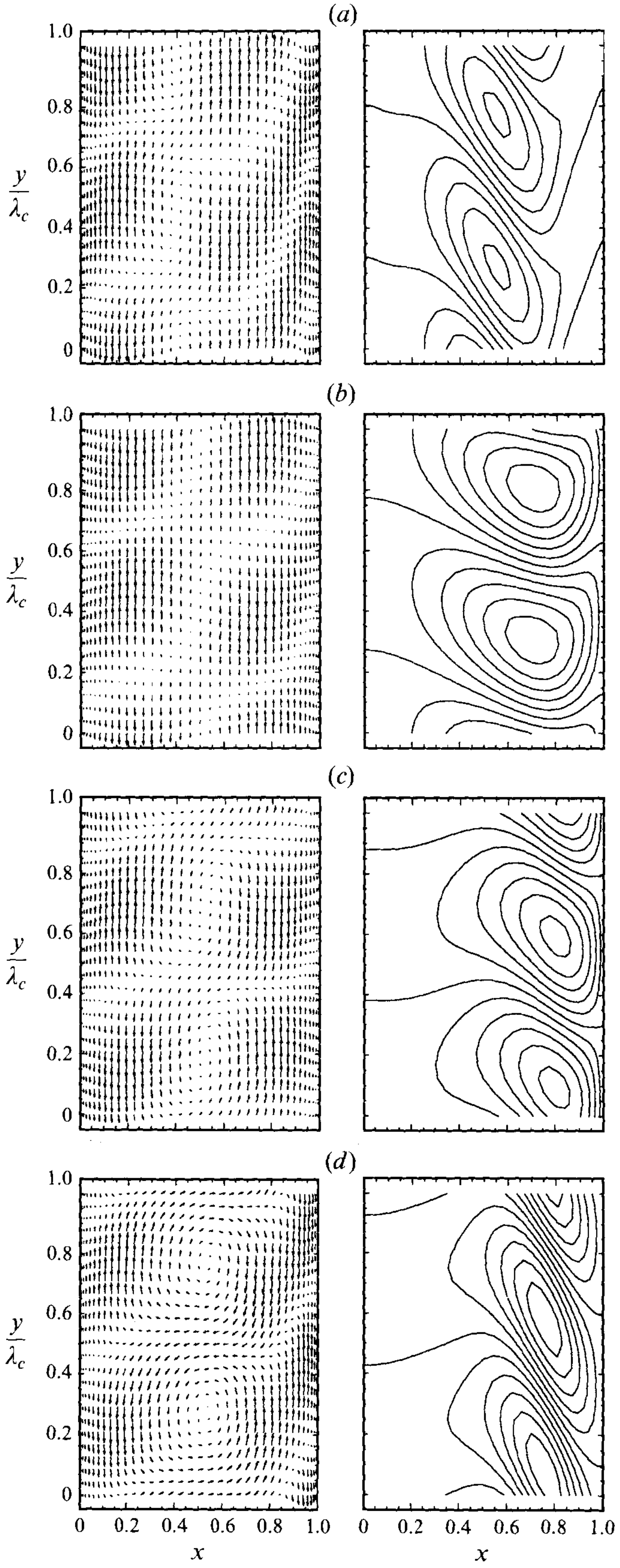

FIGURE 13. For caption see facing page.

Finally, from figure 8(*a*) we observe the substantial stabilizing influence of the large temperature difference at $\epsilon = 0.6$. From figure 8(*e, f*) we observe the jumps in wavenumber and wave speed due to the switch in mode of instability between the buoyant (points E and H, see table 2) and shear (points F and G, see table 2) modes as discussed earlier. We note that upon decreasing the Reynolds number past $Re_*^- \approx -860$, the instability reverts to one due to shear. In figure 13 we show the disturbance fields corresponding to the two modes of instability at Re_*^- and Re_*^+. Note that the fields are shown for one wavelength, and their lengths are scaled by their corresponding critical values. Thus, the actual wavelengths of the buoyant modes shown in figures 13(*b*) and 13(*c*) are substantially larger than the shear modes shown in figures 13(*a*) and 13(*d*). Also note how the very weak roll pattern ($|u| \ll |v|$) corresponding to point H on the buoyant branch switches to a well-developed roll pattern at point G on the shear branch. Although not shown in figure 8(*a*) we remark that as $Gr \rightarrow 0$ the basic flow again approaches a plane-Poiseuille-like distribution (see figure 1), which is stable for at least $|Re| < 2 \times 10^5$.

6. Conclusions

We have examined the linear stability of the fully developed mixed-convection flow of air in a differentially heated tall vertical channel under non-Boussinesq conditions. The influence of the non-Boussinesq effects on the stability was studied over a large range of Grashof and Reynolds numbers. Our results are in excellent agreement with known results in the Boussinesq limit. In the non-Boussinesq limit we have shown that the stability in the various regions of parameter space is controlled by a competition between the shear mechanism associated with the temperature difference, the shear mechanism due to the pressure gradient, and a buoyancy mechanism (which becomes dominant only when $\epsilon \geqslant 0.536$) that is clearly due to large property variations. In addition, we have shown that owing to property variations, there exists a specific value of negative Reynolds numbers Re_{**} at which the shear mechanism changes and the critical disturbance switches from an essentially longitudinal one to rolls with a much smaller wavelength.

We close with some comments regarding the need for experimental verification of the predicted instabilities. As noted earlier, our results are in excellent agreement with the experimental data of Fukui *et al.* (1982) for small Reynolds numbers in the Boussinesq limit. However, we are not aware of any other mixed-convection experiments with either larger Reynolds numbers in the Boussinesq regime or with larger temperature differences for small or large Reynolds numbers. We hope that the present work will stimulate such experiments.

The research reported in this paper has been supported by the Air Force Engineering Research Initiation Grant RI-B-91-07 and by the Center for Applied Mathematics at the University of Notre Dame. The authors would also like to acknowledge Oleg V. Vasilyev for many discussions related to this work.

FIGURE 13. Disturbance velocity field and isotherms for $\epsilon = 0.6$, Gr_c, and Re_*^- and Re_*^+, corresponding to points (*a*) G, (*b*) H, (*c*) E, and (*d*) F displayed in figure 8. The vertical coordinates are normalized by their corresponding critical wavelengths $\lambda_c = 2\pi/\alpha_c$.

Appendix A

The functions entering in the basic flow solution (17), (18) are defined as follows in terms of $\tau = (\bar{T}/S_k)^{1/2}$:

$$f(\tau) = \tfrac{1}{3}\tau^3 - \tau + \tan^{-1}(\tau), \quad \beta = 2(1+S_k)\,S_k^{3/2}, \quad Q = \beta[f(\tau_c) - f(\tau_h)],$$

$$\theta(\tau) = (\tau^2 - \tau_h^2) + (S_\mu/S_k - 1)\ln[(1+\tau^2)/(1+\tau_h^2)],$$

$$\phi(\tau) = \tfrac{2}{15}(\tau^5 - \tau_h^5) + \tfrac{2}{3}(S_\mu/S_k - 1)[f(\tau) - f(\tau_h)],$$

$$\omega(\tau) = (\tau^3 - \tau_h^3) - [\tau^2\tan^{-1}(\tau) - \tau_h^2\tan^{-1}(\tau_h)] - [f(\tau) - f(\tau_h)]$$
$$+ 2(S_\mu/S_k - 1)[\tau - \tau_h + \tan^{-1}(\tau_h) - \tan^{-1}(\tau) - G(\tau) + G(\tau_h)],$$

where

$$G(\tau) = \sum_{j=1}^{\infty} \frac{(-1)^{j+1}\,2^{2j}(2^{2j}-1)}{(1+2j)\,(2j)!} B_{2j}[\tan^{-1}(\tau)]^{1+2j},$$

and

$$B_{2j} = \frac{1}{(2j+1)\,2^{2j}}\left[2j - \sum_{n=1}^{j-1} 2^{2n}\binom{2n+1}{2n} B_{2n}\right]$$

are Bernoulli numbers generated for $j = 1, 2, 3, \ldots$ and

$$\binom{m}{n} = \frac{m!}{n!(m-n)!}$$

are the binomial coefficients.

Appendix B

The terms entering on the right-hand sides of the kinetic and thermal potential energy balances (48) and (49) are given by

$$\Sigma_\Pi = \tfrac{1}{2}\langle \Pi(Du + i\alpha v)^* \rangle_R, \quad \Sigma_{uv} = -\tfrac{1}{2}\langle \bar{\rho} D\bar{v} u v^* \rangle_R, \quad \Sigma_B = \frac{1}{2}\left\langle \frac{\bar{\rho}}{\bar{T}} T v^* \right\rangle_R,$$

$$\Sigma_\mu = -\tfrac{1}{2}\alpha^2\langle \bar{\mu}(|u|^2 + \tfrac{4}{3}|v|^2)\rangle - \tfrac{1}{2}\langle \bar{\mu}(\tfrac{4}{3}|Du|^2 + |Dv|^2)\rangle + \tfrac{1}{2}\alpha\langle \bar{\mu}(uDv^* - u^*Dv)\rangle_I$$
$$-\tfrac{1}{3}\alpha\langle \bar{\mu}(vDu^* - v^*Du)\rangle_I - \tfrac{1}{2}\langle \bar{\mu}_T D\bar{v} T(Dv + i\alpha u)^* \rangle_R,$$

$$\Sigma_{Tu} = -\tfrac{1}{2}\langle \bar{\rho} D\bar{T} u T^* \rangle_R,$$

$$\Sigma_k = -\tfrac{1}{2}\alpha^2\langle \bar{k}|T|^2\rangle - \tfrac{1}{2}\langle \bar{k}|DT|^2\rangle - \tfrac{1}{4}\langle \bar{k}_T D\bar{T} D(|T|^2)\rangle.$$

REFERENCES

AUNG, W. & WORKU, G. 1986 Developing flow and flow reversal in a vertical channel with asymmetric wall temperatures. *J. Heat Transfer* **108**, 299–304.

BERGHOLZ, R. F. 1978 Instability of steady natural convection in a vertical fluid layer. *J. Fluid Mech.* **84**, 743–768.

BUSSE, F. H. 1967 The stability of finite amplitude cellular convection and its relation to an extremum principle. *J. Fluid Mech.* **30**, 625–649.

CHAIT, A. & KORPELA, A. 1988 The secondary flow and its stability for natural convection in a tall vertical enclosure. *J. Fluid Mech.* **200**, 189–216.

CHEN, Y.-M. & PEARLSTEIN, A. J. 1989 Stability of free-convection flows of variable-viscosity fluids in vertical and inclined slots. *J. Fluid Mech.* **198**, 513–541.

CHENOWETH, D. R. & PAOLUCCI, S. 1985 Gas flow in vertical slots with large horizontal temperature differences. *Phys. Fluids* **28**, 2365–2374.

CHENOWETH, D. R. & PAOLUCCI, S. 1986 Gas flow in open vertical slots with large horizontal temperature differences and arbitrary external temperature. *Phys. Fluids* **29**, 3187–3198.

CHOI, I. G. & KORPELA, S. A. 1980 Stability of the conduction regime of natural convection in a tall vertical annulus. *J. Fluid Mech.* **99**, 725–738.

DRAZIN, P. G. & REID, W. H. 1987 *Hydrodynamics Stability*. Cambridge University Press.

FUKUI, K., NAKAJIMA, M., UEDA, H. & MIZUSHINA, T. 1982 Flow instability and transport phenomena in combined free and forced convection between vertical parallel plates. *J. Chem. Engng Japan* **15**, 172–180.

GRAY, D. D. & GIORGINI, A. 1976 The validity of the Boussinesq approximation for liquids and gases. *Intl J. Heat Mass Transfer* **19**, 545–551.

HART, J. E. 1971 Stability of the flow in a differentially heated inclined box. *J. Fluid Mech.* **47**, 547–576.

HATZIAVRAMIDIS, D. & KU, H.-C. 1985 An integral Chebyshev expansion method for boundary-value problems of O.D.E. type. *Computers Maths. Applics.* **11**, 581–586.

HILSENRATH, J., BECKETT, C. W., BENEDICT, W. S., FANO, L., HODGE, H. J., MASI, J. F., NUTTALL, R. L., TOULOUKIAN, Y. S. & WOOLLEY, H. W. 1960 *Tables of Thermodynamic and Transport Properties*. Pergamon.

IMSL Inc. 1989 *IMSL Mathematical Library*. Version 1.1.

KORPELA, S. A., GÖZÜM, D. & BAXI, C. B. 1973 On the stability of the conduction regime of natural convection in a vertical slot. *Intl J. Heat Mass Transfer* **16**, 1683–1690.

KU, H.-C. & HATZIAVRAMIDIS, D. 1984 Chebyshev expansion methods for the solution of the extended Graetz problem. *J. Comput. Phys.* **56**, 495–512.

LEE, Y. & KORPELA, S. A. 1983 Multicellular natural convection in a vertical slot. *J. Fluid Mech.* **126**, 91–121.

LEE, Y., KORPELA, S. A. & HORNE, R. N. 1982 Structure of multicellular natural convection in a tall vertical annulus. In *Heat Transfer* 1982 (ed. U. Grigull, E. Hahne, K. Stephan & J. Straub), Vol. 2, pp. 221–226.

LIN, C. C. 1955 *The Theory of Hydrodynamic Stability*. Cambridge University Press.

ORSZAG, S. A. 1971 Accurate solution of the Orr–Sommerfeld stability equation. *J. Fluid Mech.* **50**, 689–703.

PAOLUCCI, S. 1982 On the filtering of sound from the Navier–Stokes equations. *Tech. Rep.* SAND82-8257. Sandia National Laboratories Rep.

ROGERS, B. B., GHOSH MOULIC, S. & YAO, L. S. 1993 Finite-amplitude instability of mixed convection. *J. Fluid Mech.* **254**, 229–250.

RUDAKOV, R. N. 1967 Spectrum of perturbations and stability of convective motion between vertical plates. *Appl. Math. Mech.* **31**, 376–383.

SUSLOV, S. A. & PAOLUCCI, S. 1995 Stability of natural convection flow in a tall vertical enclosure under non-Boussinesq conditions. *Intl J. Heat Mass Transfer* **38**, 2143–2157.

THANGAM, S. & CHEN, C. F. 1986 Stability analysis on the convection of a variable viscosity fluid in an infinite vertical slot. *Phys. Fluids* **29**, 1367–1372.

VASILYEV, O. V. & PAOLUCCI, S. 1994 Stability of unstably stratified shear flow in a channel under non-Boussinesq conditions. *Acta Mechanica* (in press).

VEST, C. M. & ARPACI, V. S. 1969 Stability of natural convection in a vertical slot. *J. Fluid Mech.* **36**, 1–15.

WHITE, F. M. 1974 *Viscous Fluid Flow*. McGraw-Hill.

YAO, L. S. & ROGERS, B. B. 1989 Mixed convection in an annulus of large aspect ratio. *J. Heat Transfer* **111**, 683–689.